



Plasmon-induced Catalytic CO₂ Hydrogenation by a Nano-sheet Pt/H_xMoO_{3-y} Hybrid with Abundant Surface Oxygen Vacancies

Journal:	<i>Journal of Materials Chemistry A</i>
Manuscript ID	TA-ART-03-2021-002277.R1
Article Type:	Paper
Date Submitted by the Author:	08-May-2021
Complete List of Authors:	Ge, Hao; Osaka University, Graduate School of Engineering, Division of Materials and Manufacturing Science Kuwahara, Yasutaka; Osaka University, Graduate School of Engineering, Division of Materials and Manufacturing Science Kusu, Kazuki; Osaka University, Graduate School of Engineering, Division of Materials and Manufacturing Science Yamashita, Hiromi; Osaka University, Division of Materials and Manufacturing Science

ARTICLE

Plasmon-induced Catalytic CO₂ Hydrogenation by a Nano-sheet Pt/H_xMoO_{3-y} Hybrid with Abundant Surface Oxygen Vacancies

Hao Ge,^a Yasutaka Kuwahara,^{*a,b,c,d} Kazuki Kusu,^a Hiromi Yamashita^{*a,b,c}

Received 00th January 20xx,
Accepted 00th January 20xx

DOI: 10.1039/x0xx00000x

Taking full advantage of solar light to promote CO₂ hydrogenation remains a challenge in the catalysis field. Combining a degeneratively-doped metal oxide and a precious metal to obtain hybrids with plasmonic absorption in the visible-light region enables the high-efficiency utilization of solar light in photothermal catalysis. Herein, MoO₃ samples with different morphologies were synthesized and combined with Pt to form hybrid materials with a strong plasmonic effect. Among the Pt/MoO₃ hybrids with various morphologies, the Pt/H_xMoO_{3-y}(Sheet) hybrid displayed the best performance in the photothermal synergistic catalysis of the reverse water-gas shift (RWGS) reaction at 140 °C under visible light irradiation because of the advantages of its nanosheet structure (e.g., a high specific surface area, high proportion of exposed surface atoms, and good optical transparency). The Pt/H_xMoO_{3-y}(Sheet) catalyst outperformed Pt/H_xMoO_{3-y} hybrids with a bulk, belt, or rod morphology. Thermogravimetry, UV-vis-NIR diffuse reflectance spectroscopy, and model reactions demonstrated that the Pt/H_xMoO_{3-y}(Sheet) hybrid contained the largest amount of surface O vacancies and exhibited the strongest plasmonic absorption, which are the primary reasons for its highest catalytic activity among the investigated hybrid catalysts. Photoelectric characterization revealed that the Pt/H_xMoO_{3-y}(Sheet) hybrid could generate hot electrons under visible-light irradiation. X-ray photoelectron spectroscopy measurements showed a reversible redox event of the Mo atoms, demonstrating that the O vacancies in Pt/H_xMoO_{3-y}(Sheet) acted as active sites and regenerated during the reaction. A possible mechanism is proposed for the photothermal synergistic catalysis in the RWGS reaction. The nanosheet-structured Pt/H_xMoO_{3-y} hybrid can exploit solar energy to greatly reduce energy consumption during the CO₂ hydrogenation reaction, providing a greener and energy-saving scheme for the conversion of CO₂ to CO.

1. Introduction

The need for alternative clean energy sources and pollution-free technologies is becoming urgent because of the growing energy crisis and environmental problems such as the depletion of fossil fuel reserves and the dramatic increase in atmospheric greenhouse gas concentrations^{1,2}. The catalytic conversion of carbon dioxide (CO₂) can play a key role in ameliorating the energy crisis because it enables the conversion of CO₂ into value-added chemicals and fuels. Converting CO₂ into CO via the endothermic reverse water-gas shift (RWGS) reaction is an attractive strategy³⁻⁷, because the produced CO can be used directly in the manufacture of other fuels.⁸⁻¹⁰ Various precious metals (e.g., Pt¹¹, Pd¹², and Rh¹³) and nonprecious metals (e.g.,

Cu¹⁴, and Fe¹⁵) supported on oxides have been reported to be active toward the production of CO from CO₂. This thermochemical process involves the formation of a surface bicarbonate intermediate at the interface between the metal and the support, followed by hydrogenation of the intermediate by H species dissociated on the metal.^{11,16} However, traditional thermal catalysis leads to the consumption of nonrenewable energy in the process of CO₂ conversion. Xiao et al. have reported that Rh nanoparticles enveloped within zeolite crystals with controlled nanopore environments improve the selectivity toward CO in the RWGS reaction; however, CO can only be obtained at high reaction temperatures of at least 250 °C (1 MPa).¹⁷ Other previously reported heterogeneous catalysts such as Ru/CeO₂, Fe/Al₂O₃, Ru/SiO₂, and Pd/In₂O₃ require high temperatures (200-400 °C) and pressures (3-4 MPa) to achieve a high conversion rate of CO₂.¹⁸⁻²⁴ Unlike traditional thermal catalysis, photothermal synergistic catalytic processes can use light as an inexhaustible alternative energy source, thereby minimizing energy consumption and costs while achieving maximum reaction efficiency.²⁵⁻³¹ The development of a material with good optical absorption properties that can effectively convert sunlight energy is urgently needed.

MoO₃, as an n-type semiconductor, has been widely used in catalysts, photocatalysts, and gas sensors. Stoichiometric MoO₃ can absorb only ultraviolet (UV) light because of its wide

^a Division of Materials and Manufacturing Science, Graduate School of Engineering, Osaka University, 2-1 Yamada-oka, Osaka 565-0871, Japan

^b Institute for Open and Transdisciplinary Research Initiatives (OTRI), Osaka University, 2-1 Yamada-oka, Suita, Osaka 565-0871, Japan

^c Unit of Elements Strategy Initiative for Catalysts & Batteries (ESICB), Kyoto University, Katsura, Kyoto 615-8520, Japan

^d JST, PRESTO, 4-1-8 Hon-Cho, Kawaguchi, Saitama 332-0012, Japan

*E-mail: kuwahara@mat.eng.osaka-u.ac.jp (Y. Kuwahara);

yamashita@mat.eng.osaka-u.ac.jp (H. Yamashita)

Electronic Supplementary Information (ESI) available: TEM images, XRD, UV-vis-NIR, XPS, Mo K-edge XAFS spectra, N₂ adsorption-desorption isotherms, H₂-TPR profiles, TG profiles, photocurrent measurements, CV curves and catalytic results with related samples. See DOI: 10.1039/x0xx00000x

semiconductive bandgap (3.3 eV).^{32–34} Researchers have found that doping H into MoO₃ can yield a class of reduced Mo oxides specifically hydrogen molybdenum bronzes (H_xMoO_{3–y}) that exhibit strong plasmonic absorption in the visible-light region. Our group has previously reported that H_xMoO_{3–y} synthesized by a solvothermal method shows a strong surface plasmon resonance (SPR) peak at ~680 nm. Comprehensive analysis led us to attribute the plasmonic absorption to the intercalation of H atoms into the interlayer of MoO₃, which resulted in abundant delocalized electrons in the Mo 4d band.³⁵ Recently, we reported that the plasmonic Pt/H_xMoO_{3–y} hybrid can be obtained via the H-spillover process on the MoO₃ surface.³⁶ The amounts of intercalated H atoms and O vacancies as well as the visible-light absorption intensity of the hybrid could be modulated by controlling the H₂ reduction temperature. The Pt/H_xMoO_{3–y} hybrid showed high catalytic activity in the deoxygenation of sulfoxides to the corresponding sulfides under ambient conditions, where O vacancy sites functioned as active sites for deoxygenation; in addition, a further enhancement of the activity was observed under visible-light irradiation because of the SPR-induced light absorption. H-spillover enabled the surface O vacancies of the Pt/H_xMoO_{3–y} hybrid to be regenerated to sustain its deoxygenation ability toward sulfoxide. Zhou et al. demonstrated that O vacancies in H_xMoO_{3–y} display dramatically enhanced photothermal synergistic CO₂ reduction activity under simulated sunlight (UV-vis-NIR) irradiation.³⁷ In addition, Li et al. have reported that Bi₂O_{3–x} with O vacancies generates plasmonic hot electrons during visible-light irradiation, which can achieve CO₂ reduction. Ozin et al. have demonstrated that the O vacancies in Pd@H_yWO_{3–x} nanowires act as active sites in the reaction of CO₂ conversion.^{38,39}

Given the aforementioned background information, we expected H_xMoO_{3–y} to exhibit unique catalytic activity toward the photothermal synergistic catalytic hydrogenation of CO₂ for the following reasons: (1) H_xMoO_{3–y} exhibits a strong SPR phenomenon in the vis-NIR region, resulting in an enhancement of its photothermal conversion efficiency via the absorption of vis-NIR light.⁴⁰ (2) Abundant O vacancies can effectively improve the adsorption of substrate molecules (such as CO₂) and lower the activation energy of CO₂ reduction.⁴¹ In addition, unlike photocatalysis on semiconductor photocatalysts, where photogenerated electrons are transferred from the bulk to the surface of the catalyst, the SPR effect is based on the resonance between the surface free electrons and an evanescent wave. Therefore, increasing the number of delocalized electrons on the MoO₃ surface is the key to enhancing the SPR effect. In two-dimensional (2D) materials, the surface atoms can easily escape the lattice, leading to electron compensation, electron positioning, and gap states on the surface of the material.⁴² These characteristics are expected to promote the doping of H and the generation of O vacancies on the surface of MoO₃, in turn generating abundant delocalized electrons in MoO₃, which may lead to an enhancement of the SPR effect. However, the

literature contains few reports about the influence of MoO₃ morphology on the SPR effect and their photothermal catalysis.

In the present work, we synthesized MoO₃ with four different morphologies (e.g., Bulks, Belt, Sheet, and Rod) and combined them with Pt to synthesize Pt/H_xMoO_{3–y} hybrid catalysts. The synthesized Pt/H_xMoO_{3–y} hybrids that exhibit plasmonic absorption were examined in the photothermal catalytic RWGS reaction to produce CO via CO₂ hydrogenation for the first time. With the assistance of light, the Pt/H_xMoO_{3–y}(Sheet) exhibited the highest catalytic activity among the examined Pt/H_xMoO_{3–y} catalysts because it possessed the largest number of exposed O vacancies on its surface. The Pt/H_xMoO_{3–y}(Sheet) hybrid exhibited a fourfold greater CO production rate under visible-light irradiation ($\lambda > 450$ nm) than under dark conditions. Moreover, a reversible redox reaction of Mo species during the CO₂ hydrogenation reaction over the Pt/H_xMoO_{3–y}(Sheet) was verified by X-ray photoelectron spectroscopy (XPS) measurements; this reaction ensures the regeneration of the O vacancies and sustains the catalytic activity and the plasmonic effect.

2. Experimental

2.1 Materials

(NH₄)₆Mo₇O₂₄·4H₂O (99.0%), ruthenium (III) chloride hydrate (RuCl₃·xH₂O) and tungsten (VI) oxide (WO₃) were purchased from Wako Pure Chemical Industries Ltd. K₂PtCl₄, Na₂PdCl₄, H₂AuCl₄, urea (99%), Mo powder and hydrogen peroxide (H₂O₂, 30%) were purchased from Nacalai Tesque Inc. Silica (SiO₂) as a catalyst support was purchased from Sigma-Aldrich Co.

2.2 Synthesis of MoO₃ with Different Morphology

MoO₃(Bulk): 4.0 g of (NH₄)₆Mo₇O₂₄·4H₂O was calcined at 450 °C in air with a ramping rate of 1 °C/min for 4 h. MoO₃(Sheet): 576.6 mg of Mo powder was added to 72 mL of ethanol in a 200 mL eggplant flask, and subsequently 9 mL of H₂O₂ (30%) was added and stirred for 1 h until the yellow transparent solution was obtained. Then, 40 mL of yellow transparent solution was transferred into the stainless-steel autoclave and maintained at 160 °C 18 h. The solid product was collected, washed with distilled water three times, dried overnight at 80 °C to yield nanosheet-structured MoO₃ (MoO₃(Sheet)).³⁴ MoO₃(Rod): Rod-structured MoO₃ was synthesized according to the same procedure used to prepare MoO₃(Sheet) except that acetonitrile was used as a solvent instead of ethanol. MoO₃(Belt): Mo powder (959.5 mg) and 20 mL distilled water were added to a 200 mL eggplant flask. Then 20 mL H₂O₂ (30%) was then added, and the resultant mixture was stirred for 30 min to obtain a yellow transparent solution. 40 mL of the obtained yellow transparent solution was transferred to a Teflon vessel, sealed in a stainless-steel autoclave, and maintained at 180 °C for 24 h. The solid product was collected, washed with distilled water three times, dried overnight at 80 °C to yield MoO₃ nanobelt (MoO₃(Belt)).⁴³

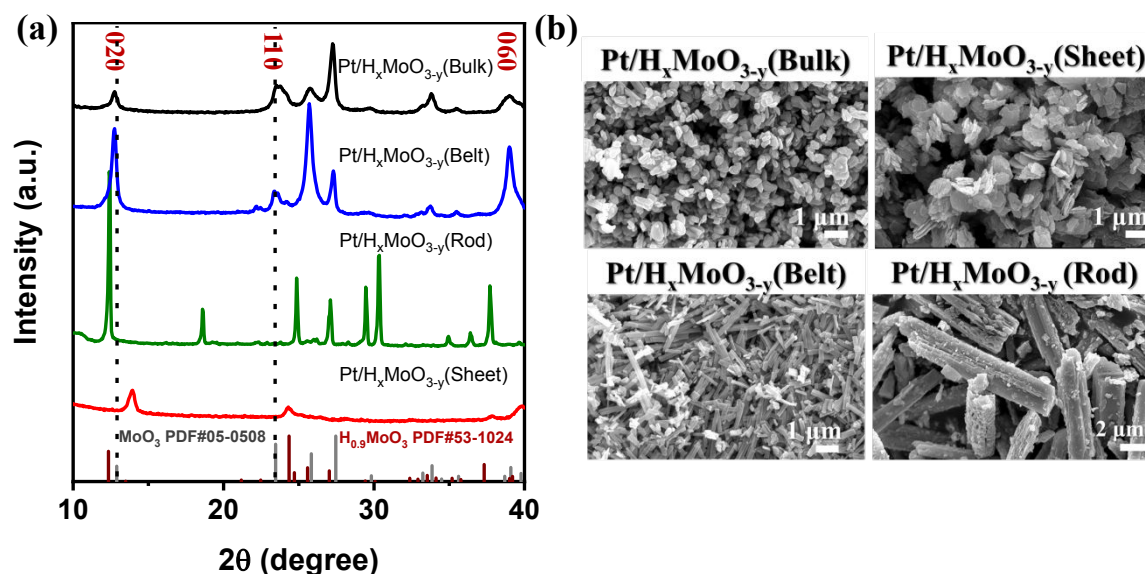


Figure 1. (a) XRD patterns and (b) FE-SEM images of Pt/H_xMoO_{3-y} with different morphologies (Bulk, Belt, Rod, Sheet).

2.3 Synthesis of Pt/H_xMoO_{3-y} Hybrid

First, 1.0 g of MoO₃(Sheet) and 0.2 g of urea were added to 80 mL distilled water. Then, 5 mL of K₂PtCl₄ solution (30 mM) was added and the resultant mixture was stirred for 6 h at 95 °C to precipitate Pt²⁺ ions. The obtained Pt/MoO₃(Sheet) was centrifuged, washed with distilled water and ethanol, and dried under vacuum at room temperature. The Pt/MoO₃(Sheet) was subsequently reduced for 30 min at 200 °C under flowing H₂ at 20 mL/min at a heating rate of 5 °C/min to obtain Pt/H_xMoO_{3-y}(Sheet). Pt/H_xMoO_{3-y} hybrids with different morphologies, including Pt/H_xMoO_{3-y}(Bulk), Pt/H_xMoO_{3-y}(Belt), and Pt/H_xMoO_{3-y}(Rod), were obtained in the same manner.

2.4 Electrochemical Measurements

Photocurrent was measured in a three-electrode system with a potential of 0 V (vs Ag/AgCl) using a HS-5000 electrochemical measurement system in 0.5 M Na₂SO₄ solution. Ag/AgCl electrode (in saturated KCl) and Pt wire were used as the reference electrode and the counter electrode, respectively. The working electrodes were prepared by mixing 5 mg of catalyst with 1.5 mL of ethanol, 0.5 mL of deionized water and 100 μL of Nafion (5%). 50 μL of the resultant mixture was extracted and placed on the FTO conductive glass to prepare a working electrode.

2.5 Characterization

X-ray diffraction (XRD) patterns were recorded using a Rigaku Ultima IV diffractometer equipped with a Cu Kα radiation source. Field-emission scanning electron microscopy (FE-SEM) images were obtained using a JEOL JSM-6500 field-emission microscope. Transmission electron microscopy (TEM) images were recorded using a Hitachi H-800 electron microscope operated at 200 kV and equipped with an energy-dispersive X-

ray spectroscopy detector. UV-vis-NIR diffuse-reflectance spectra were recorded on a Shimadzu UV-2600 spectrophotometer equipped with an integrating sphere. BaSO₄ was used as a reference. The Kubelka-Munk function was used to calculate the absorption spectrum. XPS data were recorded using a Shimadzu ESCA 3200 equipped with a Mg Kα radiation source as the excitation source. Binding energies were calibrated on the basis of the adventitious carbon (C 1s) peak at 284.5 eV. The Mo K-edge X-ray absorption fine structure (XAFS) measurements were performed in transmission mode at the BL01B1 beam line of SPring-8 (JASRI), Hyogo, Japan. A Si (311) double-crystal monochromator was used to monochromatize the synchrotron beam. The sample pellets used for the Mo K-edge XAFS measurements were prepared by mixing the catalyst with high-purity boron nitride (BN). Nitrogen adsorption-desorption measurements were carried out at -196 °C using a BELSORP-max system (MicrotracBEL). The sample was treated at 150 °C for 12 h under vacuum before the measurement. H₂ temperature-programmed reduction (H₂-TPR) measurements were carried out on a BELCAT-II (MicrotracBEL) instrument. TPR profiles were recorded at a heating rate of 5 °C/min and with the samples under a 5 vol% H₂/Ar atmosphere flowing at 30 mL/min.

2.6 Activity Evaluation

The catalyst (100 mg) after H₂ reduction was put into a glass-made batch reactor. Quartz caps were used to seal the reactor. Before starting CO₂ reduction, the H₂ flow (50 mL/min) was fed into the reactor for 20 minutes, then the temperature was raised to the reaction temperature. A mixed gas of H₂ and CO₂ (1:1 v/v) was introduced into the reactor to initiate the reaction. For photothermal CO₂ hydrogenation, reaction was performed with Xe lamp irradiation (SAN-EI ELECTRIC XEF-501S, λ > 450 nm)

using a 450 nm cutoff filter from the top of the reactor. The CO₂ and gas products were analysed and quantified using a gas chromatography (Shimadzu GC-8A) with a flame ionization detector and a methanizer (Shimadzu MTN-1) equipped with an active carbon column.

3. Result and Discussion

3.1 Characterization of MoO₃ and Hybrid of Pt/H_xMoO_{3-y}

Powder X-ray diffraction patterns of MoO₃ with different morphologies are shown in **Figure S1a**. The MoO₃(Rod) is assigned to hexagonal MoO₃ (h-MoO₃). The peaks at 12.7°, 25.7°, and 38.9° in the patterns of MoO₃(Belt), MoO₃(Bulk) and MoO₃(Sheet) can be assigned to the (020), (040) and (060) crystal planes of orthorhombic α -MoO₃. Comparing the intensities of the (020), (040), and (060) peaks in the patterns of the MoO₃(Belt), MoO₃(Bulk) and MoO₃(Sheet) reveals that, MoO₃(Belt) exposes more {010} facets, which are stable crystalline facets with fewer coordinatively unsaturated Mo atoms than other facets.⁴⁴ However, facets with high chemical stability are unreactive. Notably, the (020) peak in the pattern of the MoO₃(Sheet) sample exhibits a slight shift toward smaller angles compared with the corresponding peak in the patterns of MoO₃(Belt) and MoO₃(Bulk), indicating the intercalation of H⁺ ions during the solvothermal synthesis. **Figure 1a** shows the XRD patterns of Pt/H_xMoO_{3-y} (Sheet, Belt, Bulk, Rod) reduced

under H₂ condition at 200 °C. The shift of the (020) peak in the patterns of Pt/H_xMoO_{3-y} (Sheet, Belt, Bulk) toward smaller angles indicates the intercalation of H⁺ ions. Notably, the Pt/H_xMoO_{3-y}(Sheet) transforms from orthorhombic α -MoO₃ to monoclinic H_{0.9}MoO₃, which is attributable to the intercalation of a large amount of H atoms into the MoO₃(Sheet) matrix. The peak intensity of Pt/H_xMoO_{3-y}(Sheet) decreases dramatically, suggesting the introduction of defect sites. The peak position of Pt/H_xMoO_{3-y}(Rod) did not show any changes upon H₂ reduction, indicating that H⁺ ions are difficult to incorporate into MoO₃(Rod). **Figure S1b** displays FE-SEM images of MoO₃ nano-rod, nano-bulk, nano-sheet and nano-belt. After the reduction under H₂, as shown in **Figure 1b**, the FE-SEM images of Pt/H_xMoO_{3-y} (Sheet, Bulk, Belt) shows that their morphologies remained unchanged. The N₂ adsorption-desorption isotherms (**Figure S2a**) show that the MoO₃(Sheet) exhibits the largest surface area among the investigated morphologies, revealing that the MoO₃(Sheet) has more exposed active sites (O vacancies) on its surface, which will promote the adsorption of CO₂, as discussed later. The surface area of all the samples decreased after reduction under H₂, which could be attributed to the deposition of Pt particles (**Figure S2b**). H₂ temperature programmed reduction (H₂-TPR) profiles (**Figure S3**) verify the H-spillover process,⁴⁵⁻⁴⁸ in which the chemisorbed H₂ at the metal sites (Pt) to form reactive H atoms that can be inserted into the bulk to reduce MoO₃. The profiles of the Pt/MoO₃ (Sheet, Bulk, Belt, Rod) show obvious TPR signals. The pure

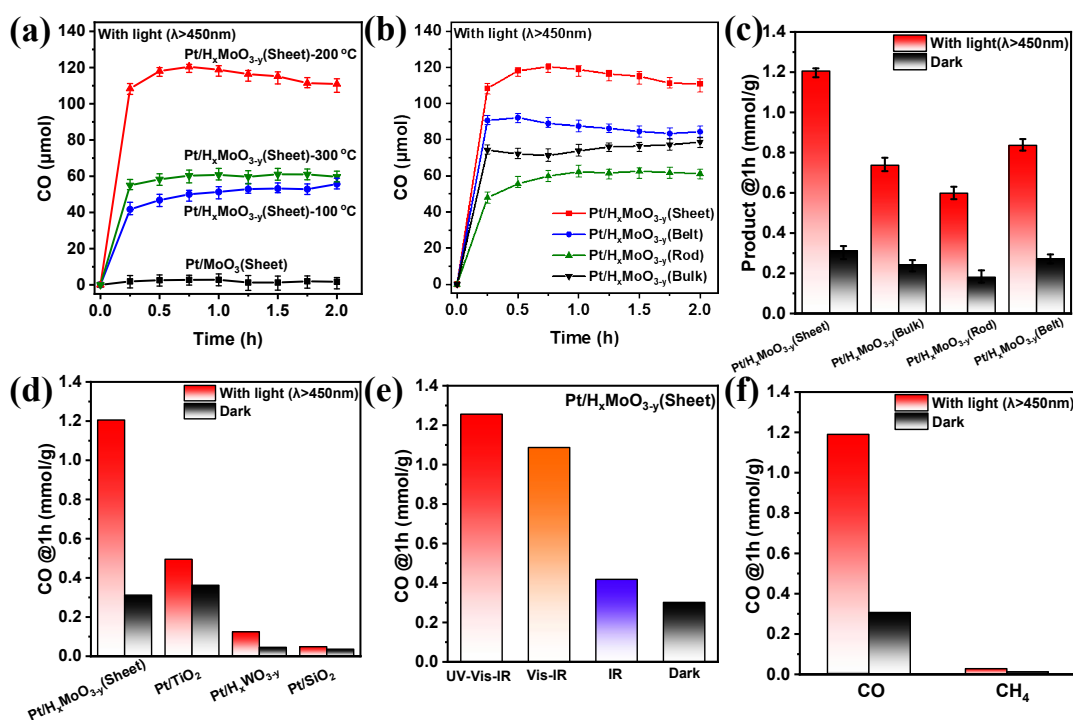


Figure 2. Catalytic activity test in the reverse water-gas shift (RWGS) reaction: (a) Pt/H_xMoO_{3-y}(Sheet) after reduction by H₂ at different temperatures under visible light ($\lambda > 450$ nm), (b) Pt/H_xMoO_{3-y} (Sheet, Belt, Rod, Bulk) after reduction by H₂ at 200 °C under visible light irradiation ($\lambda > 450$ nm). (c) Comparison of the activity under visible light irradiation and under the dark condition over the series of Pt/H_xMoO_{3-y} catalysts. (d) Comparison of the activity with different catalysts: Pt/H_xMoO_{3-y}(Sheet), Pt/TiO₂, Pt/H_xWO_{3-y} and Pt/SiO₂ (all of the catalysts were reduced at 200 °C with H₂). (e) Catalytic activity test under light irradiation with different wavelengths of light over Pt/H_xMoO_{3-y}(Sheet) catalyst. (f) Selectivity of products obtained with Pt/H_xMoO_{3-y}(Sheet) under visible light and under the dark condition. (Reaction conditions: catalyst (0.1 g), H₂: CO₂ (0.5 atm:0.5 atm), Xe lamp ($\lambda > 450$ nm), reaction temperature = 140 °C)

MoO₃(Sheet) was never reduced by H₂ in the absence of loaded Pt, which has been explained by previous work.⁴⁹ H₂ consumption associated with the reduction of the MoO₃ support with the aid of Pt particles is observed at 100–200 °C, demonstrating that the reduction of MoO₃ via H-spillover occurs at temperatures less than 200 °C. As shown in **Figure S4**, the Pt showed the strongest TPR signal at the lowest temperature range compared with other metals supported on MoO₃(Sheet), indicating that Pt has the best promotion effect for the H-intercalation and oxygen vacancies generation in the MoO₃(Sheet).

3.2 Photothermal Catalytic Activity

Adjusting the H₂ reduction temperature of Pt/MoO₃ enables control of the stoichiometry of H⁺ ions and O vacancies (O_v) in Pt/H_xMoO_{3-y}, which further influences the intensity of its plasmonic absorption and its catalytic activity.^{36, 44} **Figure 2a** shows the catalytic activities of unreduced Pt/MoO₃(Sheet) and a series of Pt/H_xMoO_{3-y}(Sheet) reduced at different temperatures. The Pt/H_xMoO_{3-y}(Sheet) reduced at 200 °C exhibits the best catalytic performance, affording 120 μmol of CO in 0.5 h of reaction at 140 °C under visible light irradiation (λ > 450 nm). By contrast, unreduced Pt/MoO₃(Sheet) was inactive under the same conditions. To determine the MoO₃ morphology most suitable for the photothermal catalytic CO₂ hydrogenation reaction, hybrids of Pt/MoO₃ with different morphologies were reduced with H₂ at 200 °C and tested in the RWGS reaction. Among the investigated morphologies, the Pt/H_xMoO_{3-y}(Sheet) showed the best catalytic performance, giving a 1.5 folds higher yield of CO than the other morphologies (**Figure 2b**). As shown in **Figure 2c**, the Pt/H_xMoO_{3-y}(Sheet) also exhibited the best performance even in the dark condition (Sheet: 0.31 mmol · g⁻¹ · h⁻¹; Bulk: 0.24 mmol · g⁻¹ · h⁻¹; Belt: 0.27

mmol · g⁻¹ · h⁻¹; Rod: 0.18 mmol · g⁻¹ · h⁻¹), which could be attributed to the exposure of more active sites (O_v) on the surface of the nanosheet structure. In addition, the Pt/H_xMoO_{3-y}(Sheet) also gave a substantial yield enhancement of CO by a factor of 4 under visible-light irradiation relative to the yield of CO under the dark condition, which was the largest rate enhancement among the investigated morphologies (Bulk: 2.9 times; Belt: 3 times; Rod: 3.2 times), indicating that the visible-light irradiation strongly promoted the RWGS reaction. Compared with other catalysts published in previous papers, our prepared catalyst (Pt/H_xMoO_{3-y}(Sheet)) exhibits an excellent activity performance in a milder reaction condition (**Table S1**). The catalytic activity is expected to be highly correlated with the concentration of O_v on the catalyst surface and with plasmonic absorption, which we will discuss later. The TEM images (**Figure S5**) and XRD patterns (**Figure S6**) show no structural differences of the Pt/H_xMoO_{3-y}(Sheet) before and after the reaction, demonstrating a structure stability of Pt/H_xMoO_{3-y}(Sheet) under the reaction conditions employed in this study. The stability test of Pt/H_xMoO_{3-y}(Sheet) in a flowing system using a fixed-bed reactor (**Figure S7a**) shows that the activity performance was maintained even after six hours of gas stream, indicating that the catalyst owns a good stability under the conditions implemented in this study. A catalytic reaction of CO₂ conversion by switching gas atmospheres (Ar+H₂ or CO₂+H₂) in the dark condition was carried out to elucidate the carbon source of the CO produced (**Figure S7b**). According to the results, there was no CO generation in a flow of Ar+H₂, and CO was produced after switching the gas from Ar+H₂ to CO₂+H₂, elucidating that the CO is derived from CO₂. To demonstrate the prominent application of Pt/H_xMoO_{3-y}(Sheet) in photothermal catalysis, the Pt/TiO₂, Pt/H_xWO_{3-y} and

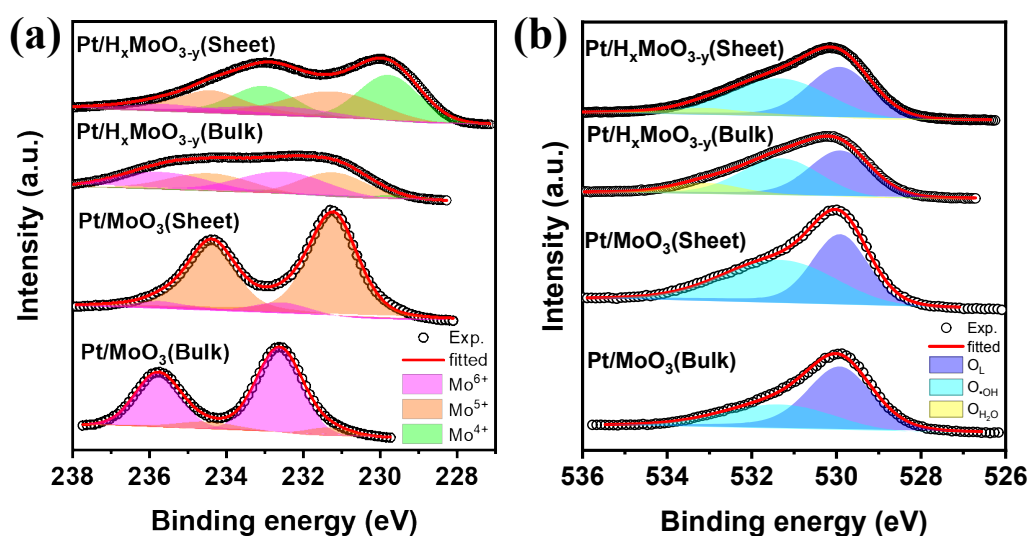


Figure 3. XPS spectra of Pt/H_xMoO_{3-y}(Sheet), Pt/H_xMoO_{3-y}(Bulk), Pt/MoO₃(Sheet) and Pt/MoO₃(Bulk): (a) Mo 3d, and (b) O 1s.

Pt/SiO₂ were prepared and tested in the RWGS reaction under identical conditions. They did not show a remarkable plasmon-induced activity enhancement (**Figure 2d**), primarily because Pt/SiO₂ and Pt/TiO₂ catalysts are not photo-responsive to visible light. The Pt/H_xWO_{3-y} exhibited a photo-enhancement phenomenon; However, its activity was much lower than that observed for Pt/H_xMoO_{3-y}(Sheet). As shown in **Figure 2e**, with the expansion of the wavelength range of the irradiated light, the yield of CO gradually increases (UV-vis-IR > vis-IR > IR). When only IR irradiation was used in the reaction, the activity increased slightly compared with the dark condition. The yield of CO increased dramatically under the vis-IR irradiation because of the strong plasmonic absorption of the Pt/H_xMoO_{3-y}(Sheet) in visible light region. The full spectrum (UV-vis-IR) irradiation further increased the yield of CO, because the Pt/H_xMoO_{3-y}(Sheet) utilizes not only the plasmonic absorption effect, but also intrinsic absorption. In addition, the Pt/H_xMoO_{3-y}(Sheet) shows the best catalytic activity with the visible light irradiation (**Figure S8**, 0.73 mmol·g⁻¹·h⁻¹), which could further prove that the photo-enhancement of the activity in CO₂ reduction mainly originates from plasmonic effect. As shown in **Figure 2f**, the selectivity of CO in the reaction was approximately 96.5%, and CH₄, which originates from the hydrogenation of CO with H atoms dissociated on Pt,⁵⁰ was hardly produced. To examine the effect of metal species, the catalytic activities of several metals (Pt, Ru, Pd, and Au) deposited onto the H_xMoO_{3-y}(Sheet) were examined in the RWGS reaction in the dark condition (**Figure S9**). The Pt/H_xMoO_{3-y}(Sheet) exhibited the highest catalytic activity at 140 °C because Pt exhibits the best ability to activate H₂ among the investigated metals. In addition, the different metals exhibited different product selectivity. Pt exhibited the highest selectivity for CO among the four investigated metals, whereas Ru was more suitable for producing CH₄ (methane selectivity: 60%).

3.3 XPS Measurements

The surface oxidation states of Pt/MoO₃ before and after H₂ reduction were analyzed by X-ray photoelectron spectroscopy (XPS). From Pt 4f XPS spectra (**Figure S10**), the Pt species in the Pt/H_xMoO_{3-y}(Sheet) and Pt/H_xMoO_{3-y}(Bulk) are predominantly reduced to Pt⁰ NPs by H₂. As shown in **Figure 3a**, the oxidation state of the Mo species in unreduced Pt/MoO₃(Bulk) was mainly Mo⁶⁺ (binding energies (BEs) at 232.5 and 235.7 eV)⁵², and that of the Mo species in the unreduced Pt/MoO₃(Sheet) was mainly Mo⁵⁺ (BEs at 231.2 and 233.4 eV) because of the intercalation of H into MoO₃ and the associated partial reduction of Mo⁶⁺ during the solvothermal synthesis. After H₂ reduction process, the XPS spectra of the Pt/H_xMoO_{3-y}(Sheet) and Pt/H_xMoO_{3-y}(Bulk) indicated the lower oxidation states of the Mo species (Mo⁴⁺: BEs at 229.8 and 233.0 eV; Mo⁵⁺: BEs at 231.2 and 234.4 eV),⁵¹ demonstrating that some of Mo⁶⁺ and Mo⁵⁺ species were reduced upon H₂ reduction. The Mo⁴⁺ concentration could be correlated with the concentration of O vacancies. The Mo K-

edge XANES spectra caused a shift of the pre-edge toward lower energies (**Figure S11**) after H₂ reduction, which is strongly related to the intercalation of H atoms into the MoO₃ (Bulk, Belt, Rod, Sheet) matrix. The Fourier transforms of extended XAFS (FT-EXAFS) spectra for the Mo K-edge (**Figure S12**) show that the peak of the Mo-(O)-Mo bond^{53,54} at ~3.1 Å becomes broad, which is likely due to the formation of a MoO_{3-x} suboxide with a large amount of O vacancies. The O 1s XPS spectra (**Figure 3b**) of unreduced Pt/MoO₃(Bulk) and Pt/MoO₃(Sheet) show peaks assignable to O_L (lattice O atoms) at 529.9 eV and O_{-OH} (-OH groups) at 531.3 eV. The peak intensity of O_{-OH} species in the spectra of the Pt/H_xMoO_{3-y}(Sheet) and Pt/H_xMoO_{3-y}(Bulk) increased, which is attributed to the generation of Mo-OH bonding after H₂ reduction at 200 °C.⁵⁵ In addition, a small peak of O_{H2O} species appeared at 533.1 eV, which is attributed to the -OH₂ groups coordinated to the Mo atoms. On the basis of the aforementioned results, we concluded that the partial Mo species are deeply reduced during the H₂ reduction. The H₂ reduction process drives the H atoms to intercalate into the orthorhombic α-MoO₃ matrixes through H₂ dissociation on Pt⁰, and the H atoms coordinate to the terminal O atoms at the interlamellar position of the orthorhombic α-MoO₃ to form Mo⁵⁺-OH bonds⁵⁶⁻⁵⁸. Notably, the proportions of (Mo⁴⁺ + Mo⁵⁺)/Mo_{total} and (O_{-OH} + O_{H2O})/O_{total} in the Pt/H_xMoO_{3-y}(Sheet) was higher than those of Pt/H_xMoO_{3-y}(Bulk) (for details, see **Table S2**), demonstrating a greater degree of reduction of the Mo oxide support and greater amounts of H atoms and O vacancies introduced for the sheet-structured MoO₃(Sheet) than for the MoO₃(Bulk), which is probably due to the unique morphology of the nanosheet-structured MoO₃ that is thinner than the bulk MoO₃.

3.4 Oxygen Vacancy Analysis

To determine the amount of oxygen vacancies and intercalated

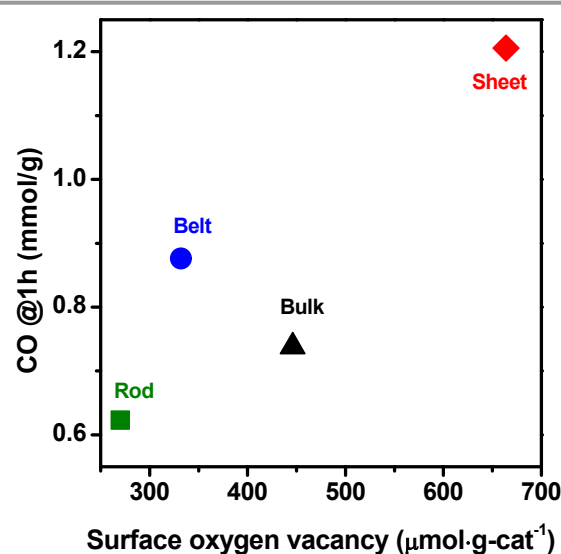


Figure 4. The relationship between the number of surface oxygen vacancies and catalytic activity.

H⁺ atoms in the series of Pt/H_xMoO_{3-y} (Bulk, Sheet, Belt, Rod), thermogravimetry (TG) was carried out in a flow of either air or N₂. The weight of H_xMoO_{3-y} is expected to change during the process of releasing intercalated H⁺ (under a N₂ environment, via thermal dehydration) and filling O_v (in air environment). From the weight changes observed during TG analysis in both environments, the stoichiometric compositions of the Pt/H_xMoO_{3-y} (Bulk, Sheet, Belt, Rod) were confirmed to be H_{1.25}MoO_{2.76} (Bulk), H_{0.81}MoO_{2.64} (Sheet), H_{0.8}MoO_{2.59} (Belt), and H_{0.9}MoO_{2.7} (Rod), respectively (Table S3) (for details, see Figure S13). According to the TG results, the amount of O vacancies in Pt/H_xMoO_{3-y} was found to increase in the order Pt/H_xMoO_{3-y}(Bulk) < Pt/H_xMoO_{3-y}(Rod) < Pt/H_xMoO_{3-y}(Sheet) < Pt/H_xMoO_{3-y}(Belt). To corroborate the aforementioned results, the deoxygenation of diphenyl sulfoxide as a model reaction was carried out. According to our previous study, sulfoxides are expected to be deoxygenated over the O vacancies on the surface of H_xMoO_{3-y} to form the corresponding sulfides.³⁴ Therefore, this reaction can be used to determine the amount of surface O vacancies of the catalyst. The Pt/H_xMoO_{3-y}(Sheet) generated the largest amount of diphenyl sulfide (664 μmol · g⁻¹ · cat⁻¹; for details, see Table S4), which indicates that Pt/H_xMoO_{3-y}(Sheet) possesses the largest amount of surface O

vacancies because of its high surface-area-to-volume ratio, as confirmed by the N₂ adsorption-desorption measurements. The concentration of surface O vacancies is closely related to the catalytic activity (Figure 4). On the basis of the aforementioned results, we concluded that the O vacancies generated in the MoO₃ during the H₂ reduction reaction act as active sites for the RWGS reaction.

3.5 Reaction Mechanism

In the CO₂ temperature-programmed desorption (CO₂-TPD) profiles (Figure 5a), peaks were observed at 350 °C and 500 °C for Pt/H_xMoO_{3-y}(Sheet); these peaks are attributed to CO₂ desorption. The profiles for Pt/H_xMoO_{3-y} (Bulk, Belt, Rod) also show different CO₂ desorption peaks. The amount of CO₂ adsorbed on the surface of Pt/H_xMoO_{3-y} (Bulk, Belt, Rod, Sheet) increased in the order Pt/H_xMoO_{3-y}(Bulk) (0.079 mmol · g⁻¹) < Pt/H_xMoO_{3-y}(Rod) (0.129 mmol · g⁻¹) < Pt/H_xMoO_{3-y}(Belt) (0.174 mmol · g⁻¹) < Pt/H_xMoO_{3-y}(Sheet) (0.37 mmol · g⁻¹), indicating that Pt/H_xMoO_{3-y}(Sheet) can adsorb the largest amount of CO₂ among the investigated catalysts due to the largest amount of oxygen vacancies exposed. The data of the CO₂ adsorption isotherms for Pt/H_xMoO_{3-y} with different morphologies are shown in Figure 5b. The Pt/H_xMoO_{3-y}(Sheet) exhibits the

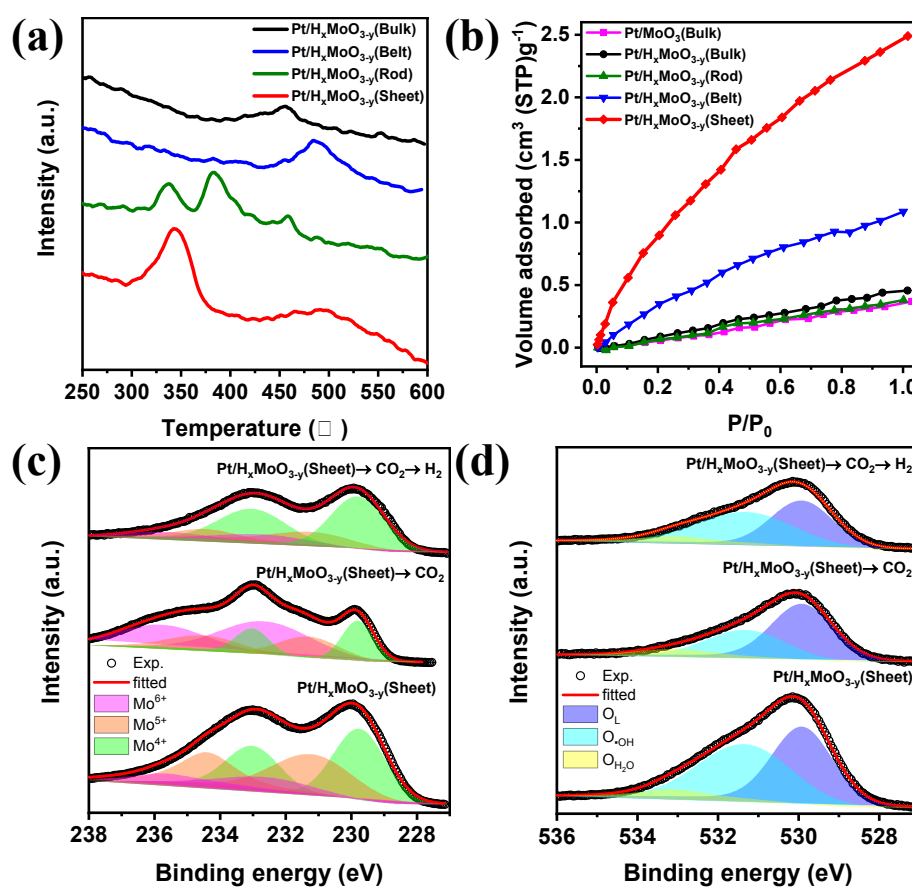


Figure 5. (a) CO₂-TPD profiles of Pt/H_xMoO_{3-y} (Bulk, Belt, Rod, Sheet). (b) CO₂ adsorption isotherms measured at 25 °C for samples of Pt/H_xMoO_{3-y} with different morphologies and unreduced Pt/MoO₃(Bulk). XPS spectra of (c) Mo 3d and (d) O 1s. (The Pt/H_xMoO_{3-y}(Sheet) was prepared by reducing the Pt/MoO₃(Sheet) at 200 °C with H₂ for 30 min; Pt/H_xMoO_{3-y}(Sheet) → CO₂ was prepared by treating the Pt/H_xMoO_{3-y}(Sheet) with CO₂ at 140 °C for 2 h; Pt/H_xMoO_{3-y}(Sheet) → CO₂ → H₂ was prepared by reducing the Pt/H_xMoO_{3-y}(Sheet) with CO₂ at 200 °C with H₂ for 30 min)

greatest CO₂ adsorption ability, which was 2-4 times greater than those of Pt/H_xMoO_{3-y} (Bulk, Belt, Rod). This greater adsorption ability of the Pt/H_xMoO_{3-y}(Sheet) is likely attributable to the increased number of surface-exposed O vacancies on the Pt/H_xMoO_{3-y}(Sheet). To investigate the reaction mechanism of the catalytic CO₂ hydrogenation, we conducted XPS measurements. As shown in **Figure 5c**, the Mo 3d XPS spectra show that, after the Pt/H_xMoO_{3-y}(Sheet) reacted with CO₂ at 140 °C for 2h in the dark condition, the peak intensity of the Mo⁴⁺ species drastically decreased; they also show that the spectra of the Pt/H_xMoO_{3-y}(Sheet) after reaction with CO₂ show a decreased proportion of (O_{-OH} + O_{H2O})/O_{total} (**Figure 5d**). These results suggest that the O vacancies of Pt/H_xMoO_{3-y}(Sheet) react with CO₂, which leads to the consumption of the surface O vacancies and to the release the intercalated H atoms. When the Pt/H_xMoO_{3-y}(Sheet) after reaction with CO₂ was reduced by H₂ at 140 °C again, the peak intensity of the Mo⁴⁺ species recovered and the proportion of (O_{-OH} + O_{H2O})/O_{total} increased (for details, see **Table S5**), which we attributed to the regeneration of O vacancies during the H₂ reduction. To further explore the role of H₂ in the reaction, the Pt/H_xMoO_{3-y}(Sheet) was treated at 140 °C for 2 h under an atmosphere of H₂ and CO₂ (0.5 atm:0.5 atm) in the dark condition. As shown in the XPS spectrum in **Figure S14**, the peak intensity of low-valent Mo species and O_{-OH} remained unchanged. The proportions of (Mo⁴⁺ + Mo⁵⁺)/Mo_{total} and (O_{-OH} + O_{H2O})/O_{total} (for details, see **Table S6**) did not show an obvious decrease, suggesting that the existence of H₂ in the reaction sustained the concentration of O vacancies so that the whole reaction could achieve reversible redox, and these evidences also demonstrate the structure stability of Pt/H_xMoO_{3-y}(Sheet).

On the basis of the aforementioned results, a possible reaction pathway is proposed. H₂ is initially adsorbed and dissociated on the surface of Pt, causing the intercalation of H atoms into the Pt/H_xMoO_{3-y}(Sheet) matrix and the generation of O vacancies in the matrix via H-spillover. The O vacancies effectively capture CO₂, which results in the deoxygenation reaction of CO₂ on the surface of Pt/H_xMoO_{3-y}(Sheet) and the generation of CO. Finally, the activated H atoms intercalate into the MoO₃ again to regenerate the O vacancy. The whole process shows the reversible redox properties of Pt/H_xMoO_{3-y}(Sheet), which can provide an effective catalytic system for photothermal catalytic CO₂ hydrogenation.

3.6 SPR-Induced Activity Enhancement

The UV-vis-NIR diffuse reflectance spectra (**Figure S15**) show that the unreduced MoO₃ (Bulk, Rod, Belt) display a response in the UV region with an absorption edge at ~400 nm, which corresponds to their wide bandgap (3.3 eV). The unreduced MoO₃(Sheet) exhibits an SPR peak at ~680 nm because of increased free electron concentration of the crystals caused by intercalated H atoms. After the H₂ reduction process, the UV-vis-NIR diffuse reflectance spectra of Pt/H_xMoO_{3-y} with different morphologies all show a prominent SPR peak in the vis-NIR region at ~630 nm (**Figure 6a**) because of the increase of the free electron concentration in the MoO₃ during the H₂ reduction. Notably, the spectra of the Pt/H_xMoO_{3-y}(Sheet) show the strongest SPR peak, indicating that, among the investigate morphologies, the Pt/H_xMoO_{3-y}(Sheet) is capable of harvesting more solar energy and should exhibit the best photo-enhancement effect in the RWGS reaction. As shown in **Figure 6b**, as the H₂ reduction temperature

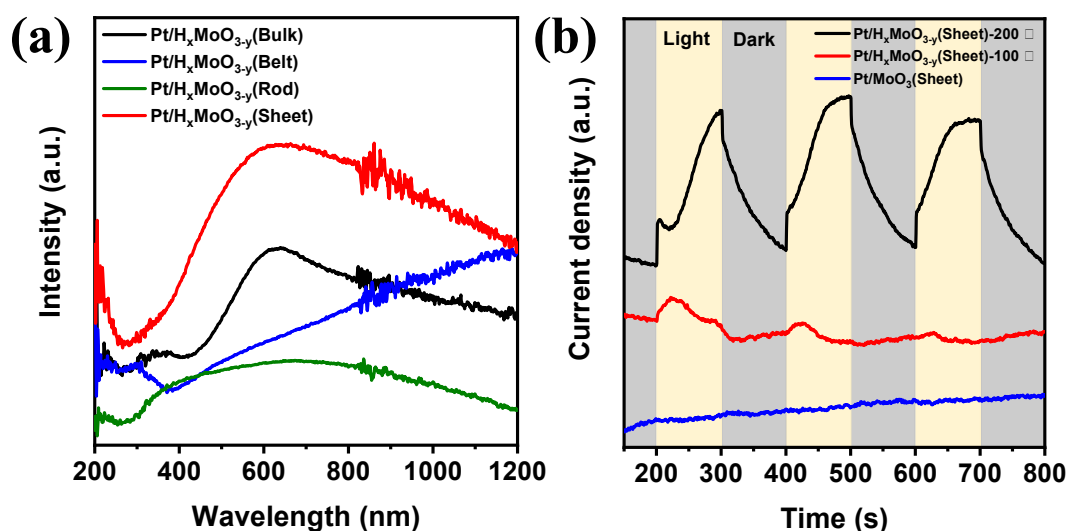


Figure 6. (a) UV-vis-NIR diffuse reflectance spectra of Pt/H_xMoO_{3-y} with different morphologies, (d) Photocurrent measurements of Pt/H_xMoO_{3-y}(Sheet) with different H₂ reduction temperatures (light source: Xe lamp ($\lambda > 450$ nm)).

increases, the photocurrent density of the Pt/H_xMoO_{3-y}(Sheet) increase, indicating that the degree of reduction of MoO₃ in the Pt/H_xMoO_{3-y}(Sheet) at elevated temperatures enhances the SPR effect. This result also indicates that the plasmon resonance of the Pt/H_xMoO_{3-y}(Sheet) can be adjusted by changing the concentration of free carriers in the MoO₃(Sheet) host. An additional important phenomenon was observed in the cyclic voltammetry (CV) (**Figure S16a**), where a strong oxidation peak of Pt/H_xMoO_{3-y}(Sheet) was observed in the first CV cycle but no oxidation peak is observed in the second cycle. This result is attributable to the oxidation of the O vacancies of Pt/H_xMoO_{3-y}(Sheet) by the positive bias (0.5–1.2 V) in the first CV cycle. The photocurrent measurement (**Figure S16b**) shows that, compared with the pristine Pt/H_xMoO_{3-y}(Sheet), the sample of Pt/H_xMoO_{3-y}(Sheet) after CV does not exhibit photocurrent response under visible-light ($\lambda > 450$ nm) irradiation. This phenomenon can be explained by the release of the intercalated H atoms and the filling of the O vacancies from H_xMoO_{3-y}(Sheet) to form semiconducting MoO₃(Sheet). Such oxidation of H_xMoO_{3-y}(Sheet) causes a decrease in the concentration of delocalized electrons, which leads to the disappearance of the plasmonic effect. Therefore, the O vacancies are not only important for CO₂ adsorption but are also necessary for maintaining the plasmonic effect of Pt/H_xMoO_{3-y}(Sheet) in the reaction.

4. Conclusion

The Pt/H_xMoO_{3-y}(Sheet) with plasmonic absorption in the visible-light region displayed a highly efficient photothermal catalysis in RWGS reaction. Comprehensive analysis demonstrated that, because of its advantageous morphology, nanosheet-structured MoO₃ favors the intercalation of H⁺/e⁻, enabling Pt/H_xMoO_{3-y}(Sheet) to generate a large amount of surface O vacancies and to exhibit strong plasmonic absorption both of which play important roles in the reaction. The Pt/H_xMoO_{3-y}(Sheet) improved the CO yield nearly fourfold under visible-light irradiation relative to the CO yield under the dark condition. In addition, a reversible redox event of Mo was verified to lead to the regeneration of O vacancies in the Pt/H_xMoO_{3-y}(Sheet) and to enhance the stability of the reaction, providing a reliable scheme for converting CO₂ to CO.

Conflicts of interest

There are no conflicts to declare.

Acknowledgements

The present work was supported by JST, PRESTO (Grant no. JPMJPR19T3), Japan. A part of this work was supported by the Iwatani Naoji Foundation, the joint usage/research program of the Artificial Photosynthesis, Osaka City University, and the

Element Strategy Initiative of MEXT, Japan (no. JPMXP0112101003). The synchrotron radiation experiments for XAFS measurements were performed at the BL01B1 beamline in SPring-8 with the approval from JASRI (nos. 2018B1185 and 2020A1064).

References

- 1 C. Hepburn, E. Adlen, J. Beddington, E. A. Carter, S. Fuss, N. Mac Dowell, J. C. Minx, P. Smith and C. K. Williams, *Nature*, 2019, **575**, 87–97.
- 2 K. Li, P. van der Poel, W. Conway, K. Jiang, G. Puxty, H. Yu and P. Feron, *Environ. Sci. Technol.*, 2018, **52**, 14538–14546.
- 3 H. Wang, J. Jia, L. Wang, K. Butler, R. Song, G. Casillas, L. He, N. P. Kherani, D. D. Perovic, L. Jing, A. Walsh, R. Dittmeyer and G. A. Ozin, *Adv. Sci.*, 2019, **6**, 1902170.
- 4 R. Long, Y. Li, Y. Liu, S. Chen, X. Zheng, C. Gao, C. He, N. Chen, Z. Qi, L. Song, J. Jiang, J. Zhu and Y. Xiong, *J. Am. Chem. Soc.*, 2017, **139**, 4486–4492.
- 5 J. H. Montoya, L. C. Seitz, P. Chakthranont, A. Vojvodic, T. F. Jaramillo and J. K. Nørskov, *Nat. Mater.*, 2017, **16**, 70–81.
- 6 L. B. Hoch, T. E. Wood, P. G. O'Brien, K. Liao, L. M. Reyes, C. A. Mims and G. A. Ozin, *Adv. Sci.*, 2014, **1**, 1400013.
- 7 J. K. Stolarczyk, S. Bhattacharyya, L. Polavarapu and J. Feldmann, *ACS Catal.*, 2018, **8**, 3602–3635.
- 8 D. U. Nielsen, X.-M. Hu, K. Daasbjerg and T. Skrydstrup, *Nat. Catal.*, 2018, **1**, 244–254.
- 9 M. Ghossoub, M. Xia, P. N. Duchesne, D. Segal and G. Ozin, *Energy Environ. Sci.*, 2019, **12**, 1122–1142.
- 10 Y.-C. Hao, Y. Guo, L.-W. Chen, M. Shu, X.-Y. Wang, T.-A. Bu, W.-Y. Gao, N. Zhang, X. Su, X. Feng, J.-W. Zhou, B. Wang, C.-W. Hu, A.-X. Yin, R. Si, Y.-W. Zhang and C.-H. Yan, *Nat. Catal.*, 2019, **2**, 448–456.
- 11 M. D. Porosoff, B. Yan and J. G. Chen, *Energy Environ. Sci.*, 2016, **9**, 62–73.
- 12 D. J. Pettigrew, D. L. Trimm and N. W. Cant, *Catal. Lett.*, 1994, **28**, 313–319.
- 13 T. Inoue, T. Iizuka and K. Tanabe, *Appl. Catal.*, 1989, **46**, 1–9.
- 14 M. Saito, J. Wu, K. Tomoda, I. Takahara and K. Murata, *Catal. Lett.*, 2002, **83**, 1–4.
- 15 J. A. Loiland, M. J. Wulfers, N. S. Marinkovic and R. F. Lobo, *Catal. Sci. Technol.*, 2016, **6**, 5267–5279.
- 16 X. Wang, H. Shi, J. H. Kwak and J. Szanyi, *ACS Catal.*, 2015, **5**, 6337–6349.
- 17 C. Wang, E. Guan, L. Wang, X. Chu, Z. Wu, J. Zhang, Z. Yang, Y. Jiang, L. Zhang, X. Meng, B. C. Gates and F.-S. Xiao, *J. Am. Chem. Soc.*, 2019, **141**, 8482–8488.
- 18 M. S. Freij, C. Mondelli, R. García-Muelas, K. S. Kley, B. Puértolas, N. López, O. V. Safonova, J. A. Stewart, D. Curulla Ferré and J. Pérez-Ramírez, *Nat. Commun.*, 2019, **10**, 3377.
- 19 M. Fan, J. D. Jimenez, S. N. Shirodkar, J. Wu, S. Chen, L. Song, M. M. Royko, J. Zhang, H. Guo, J. Cui, K. Zuo, W. Wang, C. Zhang, F. Yuan, R. Vajtai, J. Qian, J. Yang, B. I. Yakobson, J. M.

- Tour, J. Lauterbach, D. Sun and P. M. Ajayan, *ACS Catal.*, 2019, **9**, 10077–10086.
- 20 T. Riedel, G. Schaub, K.-W. Jun and K.-W. Lee, *Ind. Eng. Chem. Res.*, 2001, **40**, 1355–1363.
- 21 L. Zhang, M. R. Ball, K. R. Rivera-Dones, S. Wang, T. F. Kuech, G. W. Huber, I. Hermans and J. A. Dumesic, *ACS Catal.*, 2020, **10**, 365–374.
- 22 C. Kim, S. Hyeon, J. Lee, W. D. Kim, D. C. Lee, J. Kim and H. Lee, *Nat. Commun.*, 2018, **9**, 3027.
- 23 L. Pastor-Pérez, M. Shah, E. Le Saché and T. Ramirez Reina, *Catalysts*, 2018, **8**, 608.
- 24 A. Aitbekova, L. Wu, C. J. Wrasman, A. Boubnov, A. S. Hoffman, E. D. Goodman, S. R. Bare and M. Cargnello, *J. Am. Chem. Soc.*, 2018, **140**, 13736–13745.
- 25 S. Ning, H. Xu, Y. Qi, L. Song, Q. Zhang, S. Ouyang and J. Ye, *ACS Catal.*, 2020, **10**, 4726–4736.
- 26 X. Meng, L. Liu, S. Ouyang, H. Xu, D. Wang, N. Zhao and J. Ye, *Adv. Mater.*, 2016, **28**, 6781–6803.
- 27 C. Song, X. Liu, M. Xu, D. Masi, Y. Wang, Y. Deng, M. Zhang, X. Qin, K. Feng, J. Yan, J. Leng, Z. Wang, Y. Xu, B. Yan, S. Jin, D. Xu, Z. Yin, D. Xiao and D. Ma, *ACS Catal.*, 2020, **10**, 10364–10374.
- 28 B. Xie, R. J. Wong, T. H. Tan, M. Higham, E. K. Gibson, D. Decarolis, J. Callison, K.-F. Aguey-Zinsou, M. Bowker, C. R. A. Catlow, J. Scott and R. Amal, *Nat. Commun.*, 2020, **11**, 1615.
- 29 J. Ren, S. Ouyang, H. Xu, X. Meng, T. Wang, D. Wang and J. Ye, *Adv. Energy Mater.*, 2017, **7**, 1601657.
- 30 Z. Li, J. Liu, R. Shi, Geoffrey I. N. Waterhouse, X. Wen, and T. Zhang, *Adv. Energy Mater.*, 2021, **11**, 2002783.
- 31 M. Cai, C. Li, and L. He, *Rare Met.*, 2020, **39**, 881–886.
- 32 H. Yin, Y. Kuwahara, K. Mori, H. Cheng, M. Wen and H. Yamashita, *J. Mater. Chem. A*, 2017, **5**, 8946–8953.
- 33 H. Cheng, X. Qian, Y. Kuwahara, K. Mori and H. Yamashita, *Adv. Mater.*, 2015, **27**, 4616–4621.
- 34 H. Yin, Y. Kuwahara, K. Mori, H. Cheng, M. Wen, Y. Huo and H. Yamashita, *J. Phys. Chem. C*, 2017, **121**, 23531–23540.
- 35 H. Cheng, T. Kamegawa, K. Mori and H. Yamashita, *Angew. Chem. Int. Ed.*, 2014, **53**, 2910–2914.
- 36 Y. Kuwahara, Y. Yoshimura, K. Haematsu and H. Yamashita, *J. Am. Chem. Soc.*, 2018, **140**, 9203–9210.
- 37 J. Li, Y. Ye, L. Ye, F. Su, Z. Ma, J. Huang, H. Xie, D. E. Doronkin, A. Zimina, J.-D. Grunwaldt and Y. Zhou, *J. Mater. Chem. A*, 2019, **7**, 2821–2830.
- 38 Y. F. Li, N. Soheilnia, M. Greiner, U. Ulmer, T. Wood, A. A. Jelle, Y. Dong, A. P. Yin Wong, J. Jia and G. A. Ozin, *ACS Appl. Mater. Interfaces*, 2019, **11**, 5610–5615.
- 39 Y. Li, M. Wen, Y. Wang, G. Tian, C. Wang and J. Zhao, *Angew. Chem. Int. Ed.*, 2021, **60**, 910–916.
- 40 C. Li, T. Wang, Z.-J. Zhao, W. Yang, J.-F. Li, A. Li, Z. Yang, G. A. Ozin and J. Gong, *Angew. Chem. Int. Ed.*, 2018, **130**, 5376–5380.
- 41 Z. Ma, P. Li, L. Ye, Y. Zhou, F. Su, C. Ding, H. Xie, Y. Bai and P. K. Wong, *J. Mater. Chem. A*, 2017, **5**, 24995–25004.
- 42 F. Bai, L. Xu, X. Zhai, X. Chen and W. Yang, *Adv. Energy Mater.*, 2020, **10**, 1902107.
- 43 Q.-L. Wu, S.-X. Zhao, L. Yu, X.-X. Zheng, Y.-F. Wang, L.-Q. Yu, C.-W. Nan and G. Cao, *J. Mater. Chem. A*, 2019, **7**, 13205–13214.
- 44 J. Ziólkowski, *J. Catal.*, 1983, **81**, 311–327.
- 45 R. Prins, *Chem. Rev.*, 2012, **112**, 2714–2738.
- 46 P. A. Sermon and G. C. Bond, *Catal. Rev. Sci. Eng.*, 1974, **8**, 211–239.
- 47 S. Khoobiar, *J. Phys. Chem.*, 1964, **68**, 411–412.
- 48 S. Ladas, R. A. Dalla Betta and M. Boudart, *J. Catal.*, 1978, **53**, 356–365.
- 49 H. Cheng, M. Wen, X. Ma, Y. Kuwahara, K. Mori, Y. Dai, B. Huang and H. Yamashita, *J. Am. Chem. Soc.*, 2016, **138**, 9316–9324.
- 50 J. Ye, C. Liu, D. Mei and Q. Ge, *ACS Catal.*, 2013, **3**, 1296–1306.
- 51 M. Vasilopoulou, A. M. Douvas, D. G. Georgiadou, L. C. Palilis, S. Kennou, L. Sygellou, A. Soultati, I. Kostis, G. Papadimitropoulos, D. Davazoglou and P. Argitis, *J. Am. Chem. Soc.*, 2012, **134**, 16178–16187.
- 52 T. H. Fleisch and G. J. Mains, *J. Chem. Phys.*, 1982, **76**, 780–786.
- 53 Y.-N. Zhou, J. Ma, E. Hu, X. Yu, L. Gu, K.-W. Nam, L. Chen, Z. Wang and X.-Q. Yang, *Nat. Commun.*, 2014, **5**, 5381.
- 54 R. Radhakrishnan, C. Reed, S. T. Oyama, M. Seman, J. N. Kondo, K. Domen, Y. Ohminami and K. Asakura, *J. Phys. Chem. B*, 2001, **105**, 8519–8530.
- 55 A. Borgschulte, O. Sambalova, R. Delmelle, S. Jenatsch, R. Hany and F. Nüesch, *Sci. Rep.*, 2017, **7**, 40761.
- 56 B. Braïda, S. Adams and E. Canadell, *Chem. Mater.*, 2005, **17**, 5957–5969.
- 57 Y.-H. Lei and Z.-X. Chen, *J. Phys. Chem. C*, 2012, **116**, 25757–25764.
- 58 J. Z. Ou, J. L. Campbell, D. Yao, W. Wlodarski and K. Kalantar-zadeh, *J. Phys. Chem. C*, 2011, **115**, 10757–10763.